Chemical Science

ROYAL SOCIETY OF CHEMISTRY

EDGE ARTICLE

View Article Online
View Journal | View Issue

Cite this: *Chem. Sci.*, 2024, **15**, 7714

All publication charges for this article have been paid for by the Royal Society of Chemistry

Photo-thermal synergistic CO_2 hydrogenation towards CO over PtRh bimetal-decorated GaN nanowires/Si†

Jinglin Li,‡[a] Bowen Sheng,‡[b] Liang Qiu,‡[a] Jiajia Yang,[b] Ping Wang,*[b] Yixin Li,[a] Tianqi Yu,[a] Hu Pan,[a] Ying Li,[a] Muhan Li,[a] Lei Zhu,*[a] Xinqiang Wang,*[bcd] Zhen Huang[a] and Baowen Zhou *[a]

Photo-thermal-synergistic hydrogenation is a promising strategy for upcycling carbon dioxide into fuels and chemicals by maximally utilizing full-spectrum solar energy. Herein, by immobilizing Pt–Rh bimetal onto a well-developed GaN NWs/Si platform, CO_2 was photo-thermo-catalytically hydrogenated towards CO under concentrated light illumination without extra energies. The as-designed architecture demonstrates a considerable CO evolution rate of 11.7 mol g_{GaN}^{-1} h^{-1} with a high selectivity of 98.5% under concentrated light illumination of 5.3 W cm^{-2}, leading to a benchmark turnover frequency of 26 486 mol CO per mol PtRh per hour. It is nearly 2–3 orders of magnitude higher than that of pure thermal catalysis under the same temperature by external heating without light. Control experiments, various spectroscopic characterization methods, and density functional theory calculations are correlatively conducted to reveal the origin of the remarkable performance as well as the photo-thermal enhanced mechanism. It is found that the recombination of photogenerated electron–hole pairs is dramatically inhibited under high temperatures arising from the photothermal effect. More critically, the synergy between photogenerated carriers arising from ultraviolet light and photoinduced heat arising from visible- and infrared light enables a sharp reduction of the apparent activation barrier of CO_2 hydrogenation from 2.09 downward to 1.18 eV. The evolution pathway of CO_2 hydrogenation towards CO is also disclosed at the molecular level. Furthermore, compared to monometallic Pt, the introduction of Rh further reduces the desorption energy barrier of *CO by optimizing the electronic properties of Pt, thus enabling the achievement of excellent activity and selectivity. This work provides new insights into CO_2 hydrogenation by maximally utilizing full-spectrum sunlight *via* photo-thermal synergy.

Received 5th March 2024
Accepted 19th April 2024

DOI: 10.1039/d4sc01530d

rsc.li/chemical-science

Introduction

Recycling carbon dioxide (CO_2) backward into fuels and chemicals *via* hydrogenation is recognized as a promising strategy for the achievement of carbon neutrality, especially if green hydrogen can be massively produced from water splitting.[1–4] However, the linear molecular configuration and inert C=O bond of CO_2 (~800 kJ mol^{-1}),[5,6] together with the complex reaction network, pose tremendous challenges for efficient and selective CO_2 hydrogenation.[7,8] To date, considerable efforts have been devoted to developing various catalysts for this objective. Of note, although it is relatively favorable to produce CO compared to high-order products,[6] high temperatures, and pressures are often required to overcome the thermodynamic and kinetic barriers, which suffer from intensive thermal input and harsh operation conditions.[9–11] It is thereby desirable to explore a green pathway for fixing CO_2.

Photocatalysis presents a green strategy for CO_2 hydrogenation by using solar energy as the driving force. As a matter of fact, pure photocatalysis is usually limited by inefficient light harvesting since most of the reported photocatalysts can only respond to ultraviolet and visible photons to produce photoexcited carriers.[12,13] Infrared light, which accounts for about 53% of the solar spectrum, often remains underutilized and is often wasted as heat during photocatalysis. From the viewpoint of

[a]*Key Laboratory for Power Machinery and Engineering of Ministry of Education, Research Center for Renewable Synthetic Fuel, School of Mechanical Engineering, Shanghai Jiao Tong University, 800 Dongchuan Road, Shanghai 200240, China. E-mail: tonnyzhulei@sjtu.edu.cnmailto:; zhoubw@sjtu.edu.cn*

[b]*State Key Laboratory of Artificial Microstructure and Mesoscopic Physics, School of Physics, Nano-Optoelectronics Frontier Center of Ministry of Education (NFC-MOE), Peking University, Beijing 10087, China. E-mail: pingwang@pku.edu.cn; wangshi@pku.edu.cn*

[c]*Peking University Yangtze Delta Institute of Optoelectronics, Nantong, Jiangsu 226010, China*

[d]*Collaborative Innovation Center of Quantum Matter, School of Physics, Peking University, Beijing 100871, China*

† Electronic supplementary information (ESI) available. See DOI: https://doi.org/10.1039/d4sc01530d

‡ These authors contributed equally to this work.

energy conversion efficiency, it is critical to maximally utilize the full-spectrum sunlight for CO_2 hydrogenation.[14] Most recently, photo-thermal-synergistic catalysis has emerged as an appealing approach for breaking the bottleneck of pure photocatalysis.[13,15–19] In particular, photogenerated charges arising from ultraviolet light and heat arising from visible and infrared synergistically contribute to CO_2 hydrogenation. Despite the grand promise, there has been a lack of suitable photo-thermal-synergistic multifunctional architectures for efficient and selective CO_2 hydrogenation. What is more, the enhanced mechanism of the photo-thermal-synergistic reaction remained largely unclear.[17] Therefore, it is desirable to rationally design and construct a multifunctional architecture for addressing the issues above.

The hybrid of GaN nanowires/Si has demonstrated exceptional potential in the field of solar fuel production from CO_2 reduction[20–22] and/or water splitting,[23–25] due to the following distinct optoelectronic and catalytic properties. At first, this binary semiconductor hybrid is able to harvest a broadband range of sunlight, and simultaneously produce high-energy charges with ultraviolet photons and heating the photocatalyst through the tremendous photothermal effect of visible-/infrared-light. Meanwhile, the high structural quality, high electron mobility, and well-defined one-dimensional (1D) nanostructure are highly favorable for facilitating the separation of photogenerated carriers. What is more, the unique surface with a high area offers a flexible scaffold for loading cocatalysts to tune the behavior of various chemical species. Together, the hybrid of GaN nanowires/Si is thus promising for building a photothermal synergistic catalytic architecture for CO_2 hydrogenation. Certainly, the exploration of a rational cocatalyst is still indispensable.

Platinum (Pt) is widely recognized as a state-of-the-art hydrogenation cocatalyst because of its excellent properties for H_2 activation.[26] It is however not a suitable candidate for CO_2 hydrogenation toward CO since the strong binding strength with CO usually poisons the active sites.[27] Coupling with a secondary metal is viable for tuning the CO binding strength of Pt without compromising the superior properties of hydrogen activation,[27] thus promising to achieve efficient and durable CO_2 hydrogenation. In this work, rhodium was integrated with platinum to decorate GaN NWs/Si, assembling a multifunctional architecture (denoted as PtRh/GaN NWs/Si) for photo-thermal synergistic CO_2 hydrogenation towards CO. Profiting from the synergy between photogenerated carriers and photoinduced heat, PtRh/GaN NWs/Si significantly reduced the apparent activation energy (E_a) of CO_2 hydrogenation from 2.09 to 1.18 eV. As a result, the architecture shows a considerable CO evolution rate of 11.7 mol g_{GaN}^{-1} h^{-1} with an impressive turnover frequency (TOF) of 26 486 h^{-1} under concentrated light irradiation of 5.3 W cm^{-2}. It is nearly 2–3 orders of magnitude higher than that of 0.032 mol g_{GaN}^{-1} h^{-1} with a TOF of 72.3 h^{-1} for pure thermal catalysis under the same temperature by external heating without light illumination. Temperature-dependent photoluminescence spectroscopy measurement, operando spectroscopic characterizations and density functional theory (DFT) calculations reveal that the remarkable photothermal effect significantly inhibited the e^-/h^+ recombination. What is more, PtRh bimetal works in synergy with GaN efficiently to bend CO_2 molecule, and meanwhile, Rh species further optimized the electronic structure of Pt to significantly reduce the energy barrier of the potential-determining step *i.e.* the desorption of *CO from 1.49 to 0.61 eV. It is critical for achieving superior CO activity and selectivity. This work provides a multifunctional architecture for maximally utilizing sunlight for CO_2 hydrogenation toward CO *via* photo-thermal synergy.

Results and discussion

The hybrid of GaN NWs/Si was grown by plasma-assisted molecular beam epitaxy under nitrogen-rich conditions as reported,[6,28,29] followed by the decoration with Pt–Rh bimetal *via* a straightforward photo-deposition. The Pt/Rh ratio can be easily tuned by adjusting the deposition conditions (ESI and Fig. S1†). As characterized by scanning electron microscopy (SEM), the epitaxial GaN NWs are vertically arranged on Si wafer, with an average length and diameter of about 700 nm and 60 nm, respectively (Fig. 1A). The well-defined one-dimensional (1D) nanostructures are conducive to the absorption of light, the reduction of photogenerated carriers' diffusion distance, and the immobilization of catalytic sites. As seen from Fig. S2,† the nanowire surface becomes rough upon modification with PtRh bimetal, while the 1D morphology remains nearly unvaried. High-angle annular dark-field scanning transmission electron microscopy (HAADF-STEM) characterization shows that PtRh nanoparticles are randomly distributed on GaN NWs surface (Fig. 1B), with an average diameter of about 11.1–12.9 nm (Fig. S3†). The lattice spacing of 0.26 nm is attributed to the (002) plane of GaN (Fig. 1B),[29] which is well matched with the X-ray diffraction (XRD) results (Fig. S4†), indicating that the growth direction of GaN NWs is *c*-axis. The lattice spacing of 0.18 nm and 0.22 nm are assigned to the (002) lattice plane of metallic Rh (Rh^0)[30] and the (111) lattice plane of metallic Pt (Pt^0),[31,32] respectively (Fig. 1B).[30,31] Moreover, the energy dispersive X-ray spectroscopy (EDS) mapping further confirmed that PtRh NPs were successfully dispersed on GaN scaffolds (Fig. 1B). Nevertheless, the diffraction peaks of both Pt and Rh were not detected in the XRD pattern, which may be due to its high dispersion and low content (Table S1†). The characterization results above suggest the success in assembling the multifunctional architecture of PtRh/GaN NWs/Si.

To investigate the surface composition and electronic interaction, X-ray photoelectron spectroscopy (XPS) measurements were carried out (Fig. S5†). Typically, the characteristic peaks belonging to Ga 3d and N 1s were located at ~20 and ~397 eV, respectively (Fig. S5B and S5C†).[28,29] As shown in Fig. 1C, the HR-XPS spectra of Pt 4f in PtRh/GaN NWs/Si confirmed the presence of metallic Pt species at 71.7 eV along with a satellite peak.[33] The typical peaks of Rh 3d were located at 306.5 and 309.4 eV, respectively (Fig. 1D).[34] Of note, it is found that an obvious shift (0.2 eV) of binding energy in HR-XPS spectra of Ga 3d and N 1s after the immobilization of PtRh (Fig. S5B and S5C†), indicating the redistribution of electron

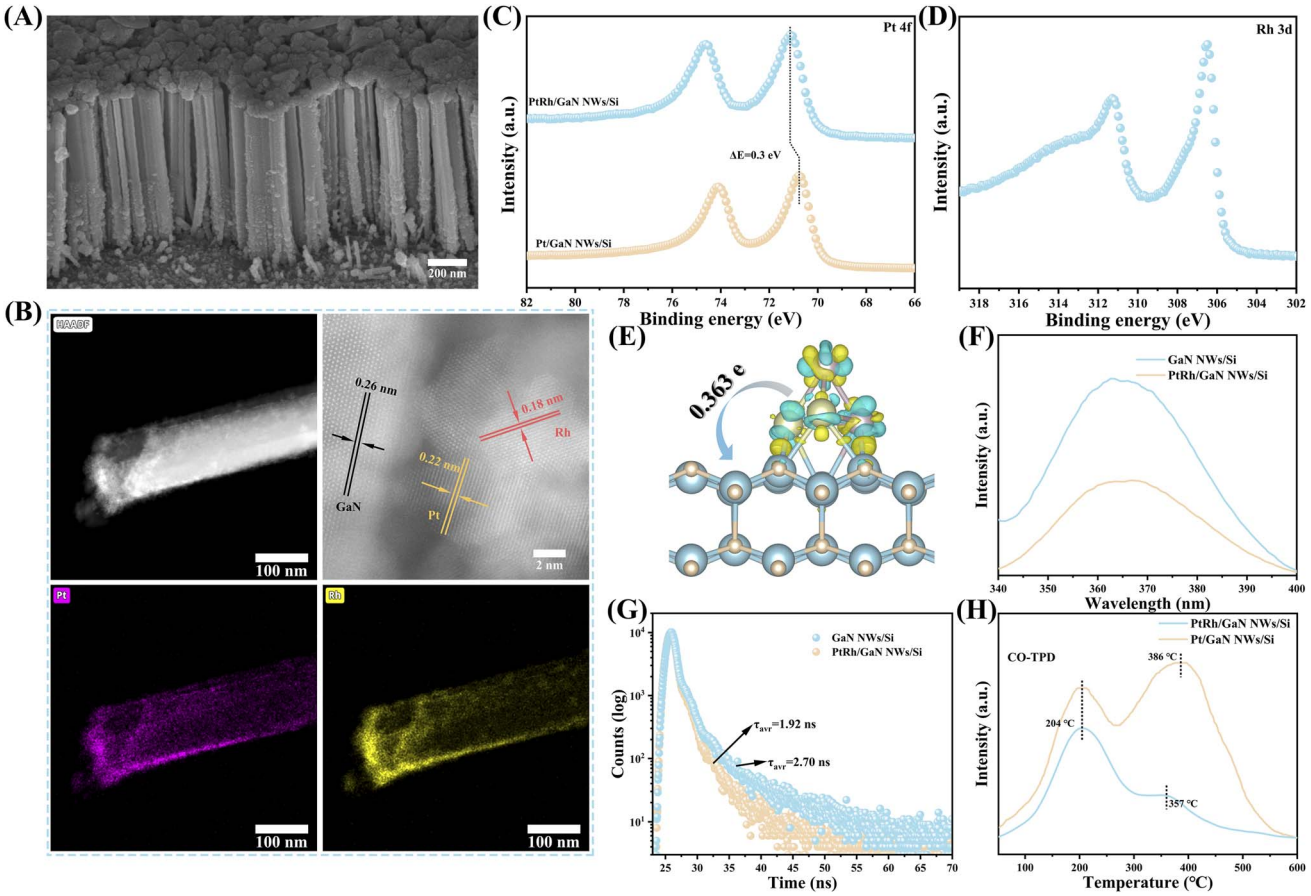

Fig. 1 (A) A 45°-tilted SEM image of PtRh-decorated GaN NWs/Si. (B) HADDF-STEM and EDS mapping images of PtRh-decorated GaN NWs/Si at various resolutions. High-resolution XPS of (C) Pt 4f and (D) Rh 3d. (E) Bader charge analysis between PtRh and GaN. The yellow and cyan regions indicate the gain and loss of electronic charge respectively, with an isosurface of 0.01 e $Å^{-3}$. Ga, blue; N, orange; Pt, green; and Rh, purple. (F) PL spectroscopy of GaN NWs/Si and PtRh/GaN NWs/Si recorded with pulse excitation of 80 MHz at a wavelength of 325 nm. (G) TR-PL spectroscopy of GaN NWs/Si and PtRh/GaN NWs/Si by a time-correlated single photon counting technique. (H) CO temperature-programmed desorption (CO-TPD) spectra of Pt/GaN NWs/Si and PtRh/GaN NWs/Si.

density between GaN and PtRh. Bader charge analysis was carried out to further confirm the XPS results. As shown in Fig. 1E, significant charge transfer from PtRh to GaN on the optimized geometry of PtRh/GaN was observed with a calculated value of 0.363e. Moreover, the incorporation of Rh results in a positive shift in the binding energy of Pt (Fig. 1C), indicating a transformation in the electronic structure of Pt. Such electronic interaction can affect the reaction by offering electron-transmission channels and tuning the surface chemical behavior upon light illumination, thus catalytically facilitating CO_2 hydrogenation. It will be studied by *in situ* irradiation XPS (ISI-XPS) and DFT calculation below. Photoluminescence (PL) spectra were conducted to investigate the e^-/h^+ recombination of the architecture. As observed from Fig. 1F, the typical peak intensity of GaN at ~365 nm was sharply lowered after decorating with PtRh, suggesting an efficient inhibition of the e^-/h^+ recombination.[35] Time resolution PL (TRPL) spectra were employed to further study the charge properties. As shown in Fig. 1G, the average lifetime of photogenerated carriers (τ_{avr}) of GaN decreased from 2.70 ns to 1.92 ns by decorating with PtRh, suggesting a faster transfer process.[35,36] The above results demonstrate that the electronic properties of the semiconductor hybrid can be improved by the incorporation of PtRh bimetal, which is favorable for light-driven CO_2 hydrogenation towards CO. What's more, the desorption of CO on Pt/GaN NWs/Si and PtRh/GaN NWs/Si was also studied, respectively. It is found that the CO over PtRh/GaN NWs/Si showed a much lower desorption temperature of 357 °C compared to Pt/GaN NWs/Si (Fig. 1H), indicating that the optimization of the electronic structure of Pt by Rh may have a positive effect on the desorption of CO. It is critical for the superior activity and selectivity of light-driven CO_2 hydrogenation toward CO, which will be further studied in the subsequent DFT calculations. Moreover, the adsorption of H_2 on the Pt or PtRh decorated-GaN NWs/Si were further studied. As shown in Fig. S6,† after coupling with Rh, the adsorption of H_2 over the architecture was significantly improved, thus facilitating the subsequent hydrogenation process.

The performance was evaluated in a homemade sealed quartz chamber under atmospheric pressure of CO_2/H_2 mixture. A 300 W Xenon lamp equipped with a quartz lens was employed as the light source. From the technological and

economic points of view, sunlight can be concentrated by a simple and cheap lens, which is beneficial for photo-thermal-synergetic CO_2 hydrogenation in practice by improving the performance and reducing the usage of photocatalyst and land. The synergistic effect between Pt and Rh was first investigated (Fig. 2A). Compared to either Pt or Rh, PtRh bimetal shows a critical improvement in CO evolution rate over GaN surface, which is up to 0.82 mol g_{GaN}^{-1} h^{-1} when the ratio of Pt and Rh is optimized to be around 1 : 1. What's more, the loading amount of PtRh also considerably influenced the activity (Fig. S7†). The CO evolution rate increases with the increasing amount of PtRh, and reaches 2.02 mol g_{GaN}^{-1} h^{-1} at an optimal PtRh amount of 0.11 μmol cm^{-2}. However, overloading PtRh led to a significant decrease in CO activity, which may be attributed to the size effect and the light-shielding effect caused by the agglomeration of active sites (Fig. S8†).[37]

The light-dependent CO activity was measured (Fig. 2B). By tuning the light intensity from 2.3 to 5.3 W cm^{-2}, the CO evolution rate exhibits an increasing trend, reaching a benchmark value of 11.65 mol g_{GaN}^{-1} h^{-1}. Owing to the high atom utilization efficiency of PtRh, a considerable turnover frequency (TOF) of 26 486 h^{-1} with a CO_2 conversion rate of 3.7% was achieved (Fig. 2B, S9, and S10). The performance is nearly 1–2 orders of magnitude higher than state-of-the-art systems for light-driven CO_2 hydrogenation toward CO recorded under comparable experimental conditions (Table S2†). Considering the thermal effect that cannot be ignored under concentrated light irradiation, the surface temperature of the architecture was measured by an infrared thermograph (Fig. S11†). It is found that the maximum surface temperature of the architecture (T_{max}) at 5.3 W cm^{-2} is as high as 349.6 °C, validating the remarkable photo-thermal effect under concentrated light illumination. To decouple the contribution of photocatalysis and thermocatalysis, the activity of pure thermocatalysis was measured at set temperatures by external heating, which is identical to the light-induced temperature. It is discovered that the photo-induced activity under concentrated light illumination without external heating is nearly 2–3 orders of magnitude higher than that of pure thermal catalysis. This finding is indicative of the critical role of the photoexcited carriers in superior performance. Further, as calculated by the Arrhenius equation, the apparent activation energy (E_a) of CO_2 hydrogenation over the PtRh/GaN NWs/Si considerably dropped from 2.09 under dark to 1.18 eV upon light irradiation (Fig. 2C). The dependence of CO evolution rate on wavelength was further measured at a set temperature of 220 °C by external heating. As

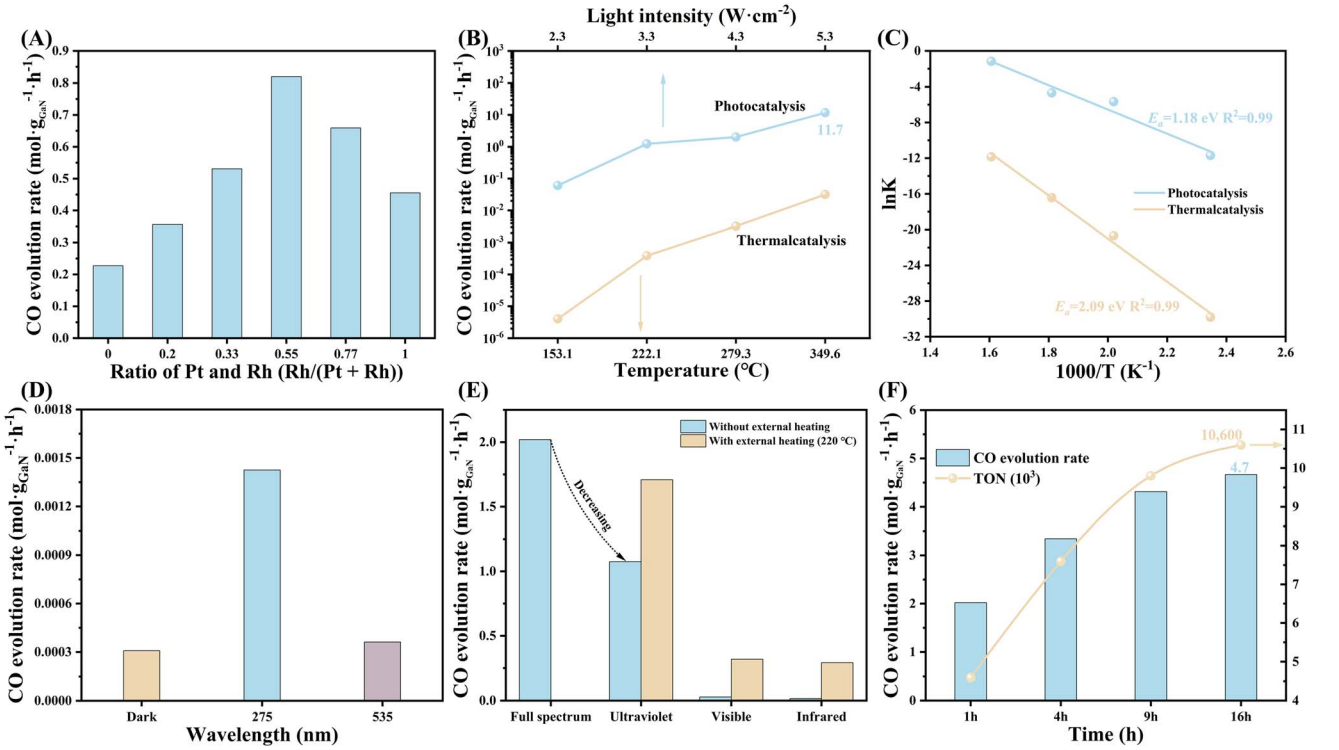

Fig. 2 (A) Influence of the ratios of Pt and Rh on CO evolution rate over PtRh/GaN NWs/Si. Light intensity, 4.3 W cm^{-2}; wafer surface area, ~0.5 cm^{-2}; density of GaN, 6.1 g cm^{-3}, volume ration of $CO_2 : H_2 = 3 : 1$; pressure, 1 atm. (B) Performance comparison between photo-thermal-synergistic catalysis and pure thermocatalysis over PtRh/GaN NWs/Si. (C) The activation energy of CO_2 hydrogenation toward CO calculated by Arrhenius plots. (D) CO evolution rate over PtRh/GaN NWs/Si under dark and monochromatic light illumination in different wavelengths. The reaction temperature under dark and light conditions was set to 220 °C by using an external temperature control system. (E) CO evolution rate over PtRh/GaN NWs/Si under light illumination in different spectral ranges (full spectra, ultraviolet, visible, and infrared) with/without an external heating source. The reaction temperature of the external heating source is set to 220 °C. (F) Durability test over PtRh/GaN NWs/Si under 4.3 W cm^{-2}. Experimental conditions for (B, D, E, and F): wafer surface area, ~0.5 cm^{-2}; density of GaN, 6.1 g cm^{-3}; PtRh, 0.11 μmol cm^{-2}; volume ratio of $CO_2 : H_2 = 12 : 1$; pressure, 1 atm.

seen in Fig. 2D, the architecture showed a CO evolution rate of 1.43 mmol g_{GaN}^{-1} h^{-1} under 275 nm. In contrast, the activity recorded at 535 nm was comparable to the pure thermocatalytic activity. Based on the discussion above, it can be seen that the photoexcited charges play a decisive role in the superior performance, and only short-wavelength photons (<365 nm) can be absorbed to produce high-energetic carriers for significantly improving CO_2 hydrogenation. To gain more insights into the photo-thermal-synergistic effect, a control experiment was conducted by using an external cooling system. As observed from Fig. S12,† the CO activity sharply dropped from 2.02 mol g_{GaN}^{-1} h^{-1} to 0.31 mol g_{GaN}^{-1} h^{-1} by alleviating the photoinduced thermal effect of the system through external cooling. The critical role of various photons was further examined. As shown in Fig. S13,† the visible and near-infrared light showed a superior photo-thermal effect, leading to the achievement of higher surface temperature *i.e.* 149.6 and 163.4 °C, respectively compared to that recorded under ultraviolet light illumination. However, without any external heat input, the CO evolution rate under ultraviolet light remained at 53.2% of that obtained under full-spectrum light illumination (Fig. 2E). In stark contrast, the introduction of only visible or near-infrared light did not show an evident improvement in the activity for the architecture compared to pure thermal catalysis. Impressively, once an external heat source was employed for heating the reaction system (220 °C), the CO activity under ultraviolet light illumination can be considerably improved to 1.71 mol g_{GaN}^{-1} h^{-1}, which is nearly 84.6% of the activity obtained under the full spectrum. The dependence of CO activity on reaction temperature by external heating under ultraviolet light illumination was further studied, and it was found that the activity increases monotonically with the reaction temperature (Fig. S14†). This finding verified the promotion of the photo-thermal effect on the reaction under visible- and infrared-light illumination. The above findings ascertain the synergetic effect between the photogenerated carriers arising from ultraviolet light and the photogenerated heat provided by visible and near-infrared light is critical for the achievement of the superior performance of CO_2 hydrogenation over PtRh/GaN NWs/Si. The durability of the architecture was also measured. A total turnover number (TON) of 10 600 mol CO per mol PtRh (Fig. 2F). As characterized by SEM, the collapse of nanowires and the shedding of active sites may be the main reasons for the activity degradation (Fig. S15 and S16†).

Temperature-dependent PL (TD-PL) spectroscopy was employed for further investigating the photo-thermal-synergistic effect. As shown in Fig. 3A, the characteristic peak intensity shows a consecutive decrease as the measured temperature increased from 50 °C to 450 °C. The internal quantum efficiency (IQE) was calculated through the integrated intensity ratio of the PL spectra recorded at 50 °C and 450 °C,[38] respectively, it is found that the IQE at 450 °C is around 3.5 times that at 50 °C. That means the recombination of the photogenerated electron–hole pairs of GaN can be effectively inhibited by the photo-thermal effect, allowing more carriers to participate in the catalytic reaction.[39] To study the evolution path of CO_2 hydrogenation towards CO over PtRh/GaN NWs/Si, *operando* diffuse reflectance infrared Fourier-transform spectroscopy (DRIFT) measurement was conducted. Typically, the characteristic peaks located at around 2360 cm^{-1} were assigned to adsorbed CO_2 (Fig. 3B).[40–42] Meanwhile, the characteristic peak of *COOH was observed at 1647 cm^{-1},[43–45] and the peak intensity increased with the continuous irradiation of light. What's more, the peaks located around 2100 cm^{-1} were associated with gas CO or *CO intermediate.[40] Herein, it is worth noting that the DRIFT spectrum of pure thermal catalysis is similar to that of photo-thermal synergistic catalysis (Fig. S17†), indicating that light illumination did not change the reaction pathway. The change of the tangent slope of the characteristic peak belonging to the *COOH intermediate in the *operando* DRITFS was calculated to describe the accumulation rate of *COOH over photocatalyst (Fig. 3C).[40] The bigger of the slope, the faster accumulation rate of the *COOH intermediates. As a sharp contrast, the accumulation rate of *COOH over the architecture surface under concentrated light illumination is much faster than that under dark, further validating the enhanced contribution of photo-thermal synergistic to improving the reaction. The above results verify the feasibility of maximally using the full solar spectrum to drive CO_2 hydrogenation by taking advantage of photons at various wavelength regions (Fig. 3D).

A high proportion of H_2 in the reactant may lead to the deep reduction of CO_2, while a high proportion of CO_2 may not be favorable for the subsequent hydrogenation. Therefore, the influence of the CO_2/H_2 ratio was also studied. As shown in Fig. S18,† a CO evolution rate of 0.62 mol g_{GaN}^{-1} h^{-1} was achieved with a high selectivity of 94.8% when the ratio of $CO_2 : H_2$ is 1 : 1. CH_4 was the major byproduct as detected by gas chromatography. By increasing the CO_2/H_2 ratio up to 12/1, the activity and selectivity of CO were significantly improved, reaching 7.10 mol g_{GaN}^{-1} h^{-1} and 98.5%, respectively. According to our previous work,[6] the increase of CO selectivity with the increase of $CO_2 : H_2$ ratio may be assigned to the decrease of hydrogen coverage on the catalyst surface, which is unfavorable for the deep hydrogenation of CO_2. However, the reduced CO activity at a higher $CO_2 : H_2$ ratio of 18 : 1 can be attributed to the insufficient amount of H_2 for driving the CO_2 hydrogenation reaction.

The electronic properties of the architecture affected the reaction significantly. The *in situ* irradiated XPS measurement was thus conducted to monitor the redistribution of photogenerated electrons at the interface between PtRh and GaN. A slightly positive shift in the binding energy of Ga 3d and N 1s was observed (Fig. S19†). Conversely, there was an apparent negative shift in the binding energy of Pt 4f and Rh 3d under light irradiation (Fig. 4A and B). This result indicates that under light illumination, photoexcited electrons can facilely transfer from GaN to PtRh owing to be electronic interaction between GaN and PtRh as discussed above, which can be further verified by DFT calculation below. The electron-rich PtRh sites are favorable for the activation and hydrogenation of CO_2 molecules. Density functional theory calculations were further performed to better understand the reaction mechanism at the molecular level. Three representative surface models of GaN

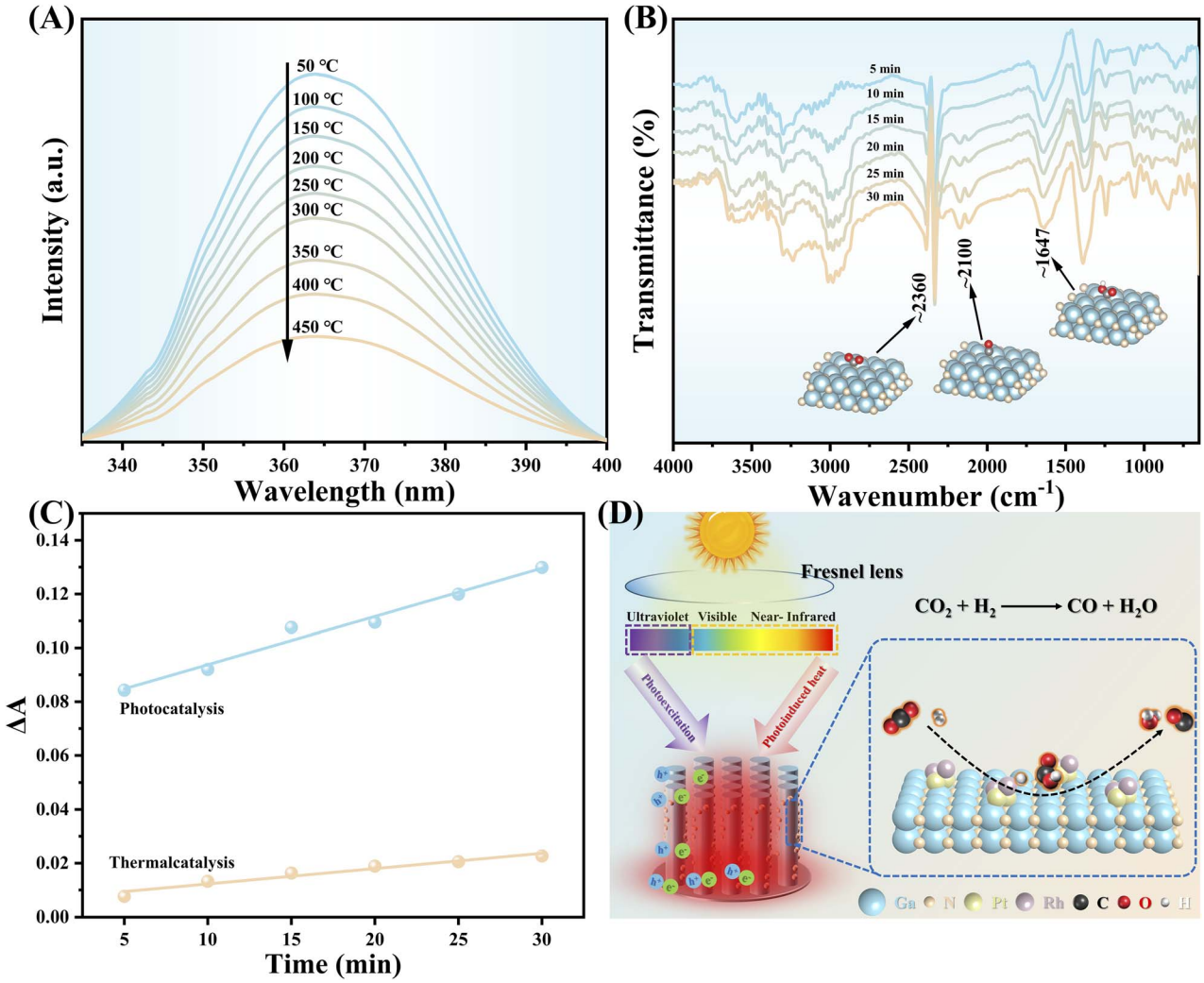

Fig. 3 (A) TD-PL spectroscopy of PtRh/GaN NWs/Si. (B) *Operando* DRIFT spectra of CO_2 hydrogenation over PtRh/GaN NWs/Si under light illumination of 4.3 W cm^{-2}. Ga, blue; N, orange; C, gray; O, red; and H, white. (C) Slope change of the peak intensity of *COOH calculated based on (B) and Fig. S17.† (D) Schematic diagram of the synergy effect of photothermal synergistic for promoting CO_2 hydrogenation over PtRh/GaN NWs/Si.

$(10\bar{1}0)$, Pt_4/GaN, and Pt_2Rh_2/GaN were first constructed (Fig. S20†). Local density of state (LDOS) was plotted to analyze the electron properties of GaN, Pt/GaN, and PtRh/GaN (Fig. 4C). The pure GaN with a large band gap (3.4 eV) is usually not conducive to electron transfer in the reaction.[46] However, after decoration with catalytic sites (Pt or PtRh), the metal state appears near the Fermi level of GaN, making this structure conductive. More importantly, the strong interaction between GaN and PtRh forms a new state of Ga and N atoms near the Fermi level at the interface, which promotes the transfer of photogenerated electrons from GaN to PtRh for the subsequent CO_2 hydrogenation, being well matched with the ISI-XPS characterization above.

The activation of CO_2 plays a pivotal role in the subsequent hydrogenation process. In this context, the adsorption characteristics of CO_2 over various surfaces including GaN $(10\bar{1}0)$, Pt_4/GaN, and Pt_2Rh_2/GaN were studied (Fig. 4D and S21†). Comparative analysis revealed significant alterations in the adsorption geometry of CO_2 upon interaction with the three surfaces. Typically, compared to the original linear configuration in the gas phase, obvious CO_2 bending with C=O bond elongation was observed on all three surfaces, with the C atom attaching to the N atom, while the O atom bonded with the Ga atom. On bare GaN, the CO_2 molecule exhibited a bent angle of 130.1° with the suspended C–O bond length of 1.250 Å, indicating the unique catalytic properties of GaN for CO_2 activation even in the absence of cocatalyst. (Fig. S21†). Upon loading monometallic Pt, the bond angle of CO_2 was further deformed to 127.95°, accompanied by an increase in the suspended C=O bond length to 1.281 Å (Fig. S21†). Coupling with Rh further elongated the C=O bond length to 1.292 Å (Fig. 4D). These findings suggest that binary PtRh works in synergy with GaN for efficient activation of the linear CO_2 molecule, thus facilitating the subsequent reactions of CO_2 hydrogenation. To further verify the promotion effect of the introduction of Rh species on the reaction, the Gibbs free energy diagram of the reaction

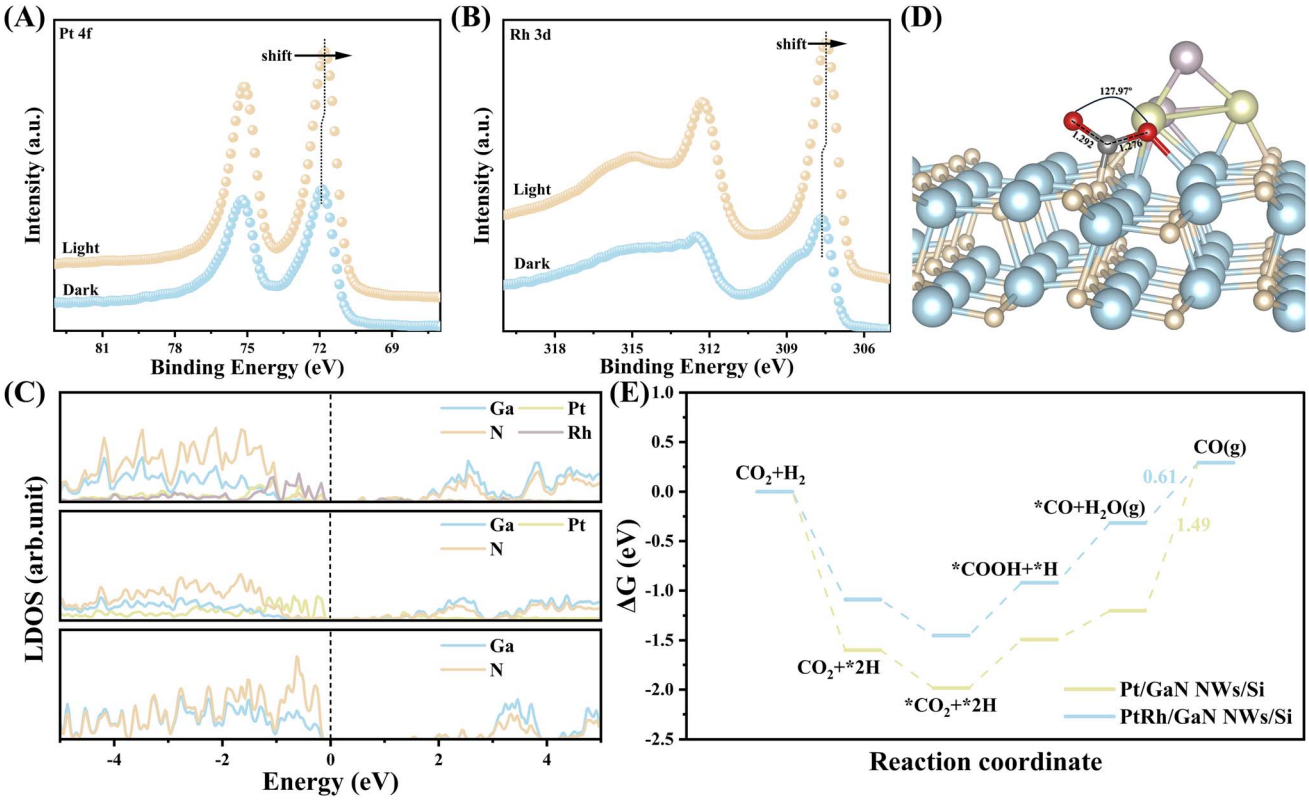

Fig. 4 ISI-XPS spectra of (A) Pt 4f and (B) Rh 3d with or without light illumination. (C) LDOS for pristine GaN, Pt_4/GaN, and Pt_2Rh_2/GaN, respectively. The black dashed line indicates the position of the Fermi level. (D) CO_2 adsorption configuration over Pt_2Rh_2/GaN. Ga, blue; N, orange; Pt, green; Rh, purple; C, gray; O, red; and H, white. (E) The calculated free energy (ΔG) diagrams for CO_2 hydrogenation on pristine GaN, Pt_4/GaN, and Pt_2Rh_2/GaN.

involving various intermediates on monometallic Pt and PtRh bimetal decorated-GaN NWs/Si were respectively calculated (Fig. S22 and S23†). As shown in Fig. 4E, compared with PtRh, the decoration of Pt alone makes the adsorption of CO_2 molecules on the catalytic interface more energetically favorable. However, the catalyst showed a higher energy barrier of 1.49 eV for *CO desorption owing to the strong *CO binding strength of Pt species. It is thus unfavorable for the formation of CO. Fortunately, the incorporation of Rh species can weaken the CO binding strength of Pt, thus enabling a significantly reduced desorption energy barrier of *CO (0.61 eV). It is well matched with the CO-TPD results. The spectroscopic and theoretical investigations together reveal the outstanding activity and selectivity of PtRh-decorated GaN NWs/Si for CO_2 hydrogenation toward CO.

Conclusion

In summary, a photo-thermal-synergistic architecture was explored for CO_2 hydrogenation by assembling a binary PtRh cocatalyst with GaN NWs/Si. Under concentrated light illumination, the synergy between photogenerated carriers and photoinduced heat enables a sharp reduction of the apparent energy of CO_2 hydrogenation from 2.09 downward to 1.18 eV. It thus results in a considerable CO evolution rate of 11.7 mol g_{GaN}^{-1} h^{-1} with a high TOF value of 26 486 h^{-1} and a high selectivity of 98.5% without extra energies. Control experiments, various spectroscopic characterizations, and density functional theory calculations verified the origin of the superior performance and the enhanced photo-thermal mechanism. The evolution pathway of CO_2 hydrogenation towards CO was disclosed at the molecular level. This work shows a study of maximally utilizing the full spectrum of sunlight for CO_2 hydrogenation toward CO by photo-thermo-synergistic catalysis.

Methods

MBE growth of GaN NWs/Si

Pristine GaN NWs were epitaxially grown on a 4-inch silicon (111) wafer using a plasma-assisted molecular beam epitaxy (SVTA MBE) system under nitrogen-rich conditions. Initial processing involved standard high-temperature pre-growth degassing and nitridation. Subsequently, nanowire growth ensued at a constant nitrogen flux and a growth temperature of 700 °C. The resulting nanowires exhibit a p–n double-layer structure. Magnesium (Mg)-doped p-GaN layers were grown using successive steps of Mg temperatures of 230 °C, 250 °C, and 270 °C. Remarkably, the nanowires were formed simply by turning on the Mg flux during continuous growth without any interruption in growth.

Photodeposition of PtRh bimetal on GaN NWs/Si

The deposition of PtRh bimetal was carried out in a 0.44 L sealed Pyrex chamber with a quartz lid. The GaN NWs/Si were fixed at the bottom of the chamber. 60 mL methanol aqueous solution (volume ratio of CH_3OH/H_2O = 1/5), and desired amounts of Pt ($PtCl_6 \cdot 6H_2O$, Shanghai Titan Technology Co., Ltd) and Rh precursors (Na_3RhCl_6, Shanghai Bailingwei Chemical Technology Co., Ltd) were added into the chamber. The loading amount and ratios of Pt and Rh were controlled by adjusting the added volume of the Rh and Pt precursors, respectively, and the loading amount was quantitatively measured by the ICP-OES characterization. Then the chamber was vacuumized and filled with argon, and irradiated with a 300 W Xe lamp for 30 min. Finally, the wafer is thoroughly rinsed with distilled water and dried.

Characterization

XRD patterns were performed using a Bruker D8 Advance diffractometer. ICP-OES measurement was carried out to estimate the amount of PtRh over GaN NWs/Si by an AGILENT ICP-OES 730. SEM characterization was performed by a Quattro ESEM (Thermo Fisher). XPS was carried out by employing ESCALAB 250xi non-monochromatic Al anodes. The data was corrected using the C 1s peak located at 284.8 eV as the internal standard. PL and TR-PL spectroscopies were performed by employing an FLS980 (Edinburgh Instruments). TD-PL spectra were performed using an FLS980 (Edinburgh Instruments) with Advanced Research Systems (ARS) LT4 series standard continuous flow thermostats. HAADF-STEM images were captured by a Thermo Fisher Scientific Talos F200X S/TEM with a Super-X EDS detector and operated at 200 kV. TEM images were obtained by a JEOL 2100F microscope. TPD characterization was carried out on an Autosorb-iQ-C chemisorption analyzer (Quantachrome, USA). ISI-XPS was analyzed by ESCALAB 250xi non-monochromatic Al anodes with a 300 W Xe lamp as an irradiation source. *Operando* DRIFT characterization was performed by a Frontier FT-IR Spectrometer, PerkinElmer, with an MCT detector and a 10 cm Demountable Gas Cell. In the process of the DRIFT measurement, the photocatalysts were fixed in the Gas Cell. The mixture gas of CO_2 and H_2 was injected into the Gas Cell through a bubbling system. The background spectrum of the system was recorded when the reaction gas reached adsorption–desorption equilibrium on the photocatalyst surface. Subsequently, the Gas Cell was closed by cutting off the injection of the mixture gas. Then the photocatalyst surface was illuminated by a 300 W Xenon lamp at a light intensity of 5.3 W cm^{-2}. The DRIFT data was recorded within a certain period of time.

Performance evaluation

The performance of photocatalytic architecture was evaluated in a 0.44 L self-made sealed quartz chamber. The photocatalyst ($\sim$0.5 cm^{-2}, $\sim$0.25 mg cm^{-2}) was first fixed at the bottom of the chamber, then the chamber was vacuumed and filled with proportionally adjustable atmospheric mixture gas of CO_2 and H_2. A 300 W Xe lamp with a quartz lens was employed as the light source to irradiate the chamber for 30 minutes. During the irradiation process, the temperature over the photocatalyst surface was recorded by infrared thermography (FOTRFIC 315, Shanghai Thermal Imaging Technology Co., Ltd). The thermocatalytic experiments were conducted in a 0.25 L tube furnace in the dark. The wavelength-dependence experiments were carried out in a 0.043 L stainless-steel chamber with a top sapphire lid, and different monochromatic light illumination (275 nm and 535 nm) was used as the light source, the system temperature was controlled at 220 °C by an external heating module. The light intensities of monochromatic light at wavelengths of 275 and 535 nm are determined as 29.8 and 285.1 mW cm^{-2}, respectively. For all wavelength-dependence measurements, the calculated light irradiation area was determined to be the area of the photocatalyst (0.25 cm^{-2}), and the reaction time was controlled at 3600 s. The products were analyzed using a gas chromatograph (GC-9080, Sun) with a thermal conductivity detector (TCD). The product evolution rate, TOF, and TON were calculated according to the following equations:

$$\text{Product evolution rate} = \frac{\text{Product yield per unit area of catalyst per hour}}{\text{Mass of catalyst per unit area}} \quad \text{(S1)}$$

$$\text{Mass of catalyst per unit area} = L \times \nu \times 6.1\ \text{g cm}^{-3} \times 1\ \text{cm}^{-2} \quad \text{(S2)}$$

where the L is the length of GaN NWs, and the ν is determined as the fill factor. According to the top-view SEM image of GaN NWs/Si (Fig. S2†), the L was estimated to be $\sim$700 nm, and the ν was about 59.2%. Substituting the density of GaN (6.1 g cm^{-3}) into the calculation, the photocatalyst mass per unit area is estimated to be 0.25 mg. The cocatalyst mass of PtRh was not taken into calculation owing to its tiny content (<0.01 mg).

$$\text{TOF} = \frac{\text{CO evolution rate}}{\text{Content of immobilized PtRh nanoparticles}} \quad \text{(S3)}$$

$$\text{TON} = \frac{\text{Yield of CO}}{\text{Content of immobilized PtRh nanoparticles}} \quad \text{(S4)}$$

Computational methods

DFT[47] calculations were performed employing the Vienna *Ab Initio* Simulation Package (VASP).[48,49] The interaction between valence electrons and ions was elucidated through the projector-augmented wave (PAW) methodology.[50] Generalized gradient approximation (GGA)[51] utilizing the Perdew–Burke–Ernzerhof (PBE) functional was employed to describe the exchange correlation in the Kohn–Sham equation.[52] Wavefunctions were expanded using a plane-wave basis set with a kinetic cutoff energy of 450 eV. In slab computations, a 2 × 1 × 1 Monkhorst-Pack k-point grid sampled the Brillouin zone.[53] Throughout geometry optimization, convergence

criteria for atomic forces and total energies were established at 0.02 eV $Å^{-1}$ and 10^{-4} eV, respectively.

Upon experimental observation of the m-plane of GaN, we constructed a GaN (100) surface using a 4 × 3 supercell comprising 4 layers to faithfully represent pristine GaN. Additionally, PtRh/GaN and Pt/GaN configurations were generated by the deposition of Rh_2Pt_2 and Pt_4 clusters on GaN (100). The optimized geometries of PtRh/GaN and Pt/GaN, in both top and side views, are depicted in Fig. S20.† To prevent image interference, a minimum vacuum spacing of 25 Å was implemented along the normal direction to the surface for all slab models and along all three directions for nanoparticles. Furthermore, during structural relaxation, the bottom two layers of GaN were constrained in their bulk positions for all slab models. The calculation of the Gibbs free energy of adsorption (ΔG) was performed using the following formula:

$$\Delta G = E_{ad} + \Delta ZPE - T\Delta S \quad (S5)$$

where E_{ad} is the adsorption energy defined by:

$$E_{ad} = E_{surface+adsorbate} - E_{surface} - E_{adsorbate} \quad (S6)$$

ΔZPE and ΔS are the changes in zero-point energy and entropy during adsorption.[54,55]

Data availability

All necessary data to support the findings of this work can be found in the paper and ESI.†

Author contributions

Conceptualization: J. L., B. Z. methodology: J. L., B. S., L. Q., L. Z., X. W., H. P., B. Z. investigation: J. L., L. Q., B. S., J. Y, Y. L, T. Y, Y. L, M. L, H. P., B. Z. visualization: J. L. funding acquisition: X. W., B. Z. project administration: Z. H., B. Z. supervision: B. Z. writing – original draft: J. L., L. Q., B. Z. writing – review & editing: J. L., B. Z.

Conflicts of interest

The authors state that there are no competing interests.

Acknowledgements

The authors thank the following financial support: National Natural Science Foundation of China (22109095) National Key Research and Development Program of China (2023YFB4004900) Shanghai Pilot Program for Basic Research – Shanghai Jiao Tong University (21TQ1400207) Oceanic Interdisciplinary Program of Shanghai Jiao Tong University (SL2022MS007). B. S., P. W., and X. W. thank for the following financial support: Beijing Outstanding Young Scientist Program (BJJWZYJH0120191000103) Beijing Natural Science Foundation (Z200004) National Natural Science Foundation of China (6230031805)

References

1 N. H. M. D. Dostagir, R. Rattanawan, M. Gao, J. Ota, J.-y. Hasegawa, K. Asakura, A. Fukouka and A. Shrotri, Co Single Atoms in ZrO_2 with Inherent Oxygen Vacancies for Selective Hydrogenation of CO_2 to CO, *ACS Catal.*, 2021, **11**, 9450–9461.

2 A. Aitbekova, L. Wu, C. J. Wrasman, A. Boubnov, A. S. Hoffman, E. D. Goodman, S. R. Bare and M. Cargnello, Low-Temperature Restructuring of CeO_2-Supported Ru Nanoparticles Determines Selectivity in CO_2 Catalytic Reduction, *J. Am. Chem. Soc.*, 2018, **140**, 13736–13745.

3 M. D. Porosoff, B. Yan and J. G. Chen, Catalytic reduction of CO_2 by H_2 for synthesis of CO, methanol and hydrocarbons: challenges and opportunities, *Energy Environ. Sci.*, 2016, **9**, 62–73.

4 X. Zhao, D. Pei, Y. Yang, K. Xu, J. Yu, Y. Zhang, Q. Zhang, G. He, Y. Zhang and A. Li, Green tea derivative driven smart hydrogels with desired functions for chronic diabetic wound treatment, *Adv. Funct. Mater.*, 2021, **31**, 2009442.

5 K. An and J. Zhu, Why Does Activation of the Weaker C=S Bond in CS_2 by P/N-Based Frustrated Lewis Pairs Require More Energy Than That of the C=O Bond in CO_2? A DFT Study, *Organometallics*, 2014, **33**, 7141–7146.

6 J. Li, B. Sheng, Y. Chen, S. M. Sadaf, J. Yang, P. Wang, H. Pan, T. Ma, L. Zhu, J. Song, H. Lin, X. Wang, Z. Huang and B. Zhou, Oxynitride-surface engineering of rhodium-decorated gallium nitride for efficient thermocatalytic hydrogenation of carbon dioxide to carbon monoxide, *Commun. Chem.*, 2022, **5**, 107.

7 S. Kattel, P. Liu and J. G. Chen, Tuning selectivity of CO_2 hydrogenation reactions at the metal/oxide interface, *J. Am. Chem. Soc.*, 2017, **139**, 9739–9754.

8 Y. Li, S. H. Chan and Q. Sun, Heterogeneous catalytic conversion of CO_2: a comprehensive theoretical review, *Nanoscale*, 2015, **7**, 8663–8683.

9 M. Nordio, M. E. Barain, L. Raymakers, M. V. S. Annaland, M. Mulder and F. Gallucci, Effect of CO_2 on the performance of an electrochemical hydrogen compressor, *Chem. Eng. J.*, 2020, **392**, 123647.

10 D. Kobayashi, H. Kobayashi, K. Kusada, T. Yamamoto, T. Toriyama, S. Matsumura, S. Kawaguchi, Y. Kubota, M. Haneda and S. M. Aspera, Boosting reverse water-gas shift reaction activity of Pt nanoparticles through light doping of W, *J. Mater. Chem. A*, 2021, **9**, 15613–15617.

11 J. Zhao, Y. Bai, Z. Li, J. Liu, W. Wang, P. Wang, B. Yang, R. Shi, G. I. N. Waterhouse, X.-D. Wen, Q. Dai and T. Zhang, Plasmonic Cu Nanoparticles for the Low-temperature Photo-driven Water-gas Shift Reaction, *Angew. Chem., Int. Ed.*, 2023, **62**, e202219299.

12 E. Gong, S. Ali, C. B. Hiragond, H. S. Kim, N. S. Powar, D. Kim, H. Kim and S.-I. In, Solar fuels: research and development strategies to accelerate photocatalytic CO_2 conversion into hydrocarbon fuels, *Energy Environ. Sci.*, 2022, **15**, 880–937.

13 Y. Peng, H. Szalad, P. Nikacevic, G. Gorni, S. Goberna, L. Simonelli, J. Albero, N. López and H. García, Co-doped hydroxyapatite as photothermal catalyst for selective CO_2 hydrogenation, *Appl. Catal., B*, 2023, **333**, 122790.

14 G. Li, C. Guo, M. Yan and S. Liu, Cs_xWO_3 nanorods: realization of full-spectrum-responsive photocatalytic activities from UV, visible to near-infrared region, *Appl. Catal., B*, 2016, **183**, 142–148.

15 S. Ning, H. Xu, Y. Qi, L. Song, Q. Zhang, S. Ouyang and J. Ye, Microstructure Induced Thermodynamic and Kinetic Modulation to Enhance CO_2 Photothermal Reduction: A Case of Atomic-Scale Dispersed Co-N Species Anchored Co@C Hybrid, *ACS Catal.*, 2020, **10**, 4726–4736.

16 J. Ma, J. Yu, G. Chen, Y. Bai, S. Liu, Y. Hu, M. Al-Mamun, Y. Wang, W. Gong, D. Liu, Y. Li, R. Long, H. Zhao and Y. Xiong, Rational Design of N-Doped Carbon-Coated Cobalt Nanoparticles for Highly Efficient and Durable Photothermal CO_2 Conversion, *Adv. Mater.*, 2023, **35**, 2302537.

17 C. Song, Z. Wang, Z. Yin, D. Xiao and D. Ma, Principles and applications of photothermal catalysis, *Chem Catal.*, 2022, **2**, 52–83.

18 J. Zhao, J. Liu, Z. Li, K. Wang, R. Shi, P. Wang, Q. Wang, G. I. Waterhouse, X. Wen and T. Zhang, Ruthenium-cobalt single atom alloy for CO photo-hydrogenation to liquid fuels at ambient pressures, *Nat. Commun.*, 2023, **14**, 1909.

19 C.-Y. Sun, Z.-W. Zhao, H. Liu and H.-Q. Wang, Core-shell nanostructure for supra-photothermal CO_2 catalysis, *Rare Met.*, 2022, **41**, 1403–1405.

20 B. AlOtaibi, X. Kong, S. Vanka, S. Y. Woo, A. Pofelski, F. Oudjedi, S. Fan, M. G. Kibria, G. A. Botton, W. Ji, H. Guo and Z. Mi, Photochemical Carbon Dioxide Reduction on Mg-Doped Ga(In)N Nanowire Arrays under Visible Light Irradiation, *ACS Energy Lett.*, 2016, **1**, 246–252.

21 S. Chu, P. Ou, P. Ghamari, S. Vanka, B. Zhou, I. Shih, J. Song and Z. Mi, Photoelectrochemical CO_2 Reduction into Syngas with the Metal/Oxide Interface, *J. Am. Chem. Soc.*, 2018, **140**, 7869–7877.

22 W. J. Dong, I. A. Navid, Y. Xiao, J. W. Lim, J. L. Lee and Z. Mi, CuS-Decorated GaN Nanowires on Silicon Photocathodes for Converting CO_2 Mixture Gas to HCOOH, *J. Am. Chem. Soc.*, 2021, **143**, 10099–10107.

23 B. Zhou and S. Sun, Approaching the commercial threshold of solar water splitting toward hydrogen by III-nitrides nanowires, *Front. Energy*, 2023, 1–3, DOI: **10.1007/s11708-023-0870-z**.

24 Y. Li, S. M. Sadaf and B. Zhou, Ga(X)N/Si nanoarchitecture: An emerging semiconductor platform for sunlight-powered water splitting toward hydrogen, *Front. Energy*, 2023, 1–24, DOI: **10.1007/s11708-023-0881-9**.

25 P. Zhou, I. A. Navid, Y. Ma, Y. Xiao, P. Wang, Z. Ye, B. Zhou, K. Sun and Z. Mi, Solar-to-hydrogen efficiency of more than 9% in photocatalytic water splitting, *Nature*, 2023, **613**, 66–70.

26 Z. Yang, Y. Qi, F. Wang, Z. Han, Y. Jiang, H. Han, J. Liu, X. Zhang and W. J. Ong, State-of-the-art advancements in photo-assisted CO_2 hydrogenation: recent progress in catalyst development and reaction mechanisms, *J. Mater. Chem. A*, 2020, **8**, 24868–24894.

27 W. Chen, J. Cao, W. Fu, J. Zhang, G. Qian, J. Yang, D. Chen, X. Zhou, W. Yuan and X. Duan, Molecular-Level Insights into the Notorious CO Poisoning of Platinum Catalyst, *Angew. Chem., Int. Ed.*, 2022, **61**, e202200190.

28 J. Li, B. Sheng, Y. Chen, J. Yang, T. Ma, C. You, Y. Li, T. Yu, J. Song, H. Pan, X. Wang and B. Zhou, Nickel-Iron Bimetal as a Cost-Effective Cocatalyst for Light-Driven Hydrogen Release from Methanol and Water, *ACS Catal.*, 2023, **13**, 10153–10160.

29 J. Li, B. Sheng, Y. Chen, J. Yang, P. Wang, Y. Li, T. Yu, H. Pan, J. Song, L. Zhu, X. Wang, T. Ma and B. Zhou, An Active and Robust Catalytic Architecture of NiCo/GaN Nanowires for Light-Driven Hydrogen Production from Methanol, *Small*, 2024, 2309906, DOI: **10.1002/smll.202309906**.

30 W. Chen, H. Wang, L. Mao, X. Chen and W. Shangguan, Influence of loading Pt, RhO_2 co-catalysts on photocatalytic overall water splitting over $H_{1.9}K_{0.3}La_{0.5}Bi_{0.1}Ta_2O_7$, *Catal. Commun.*, 2014, **57**, 115–118.

31 W. Zhang, H. Wang, J. Jiang, Z. Sui, Y. Zhu, D. Chen and X. Zhou, Size Dependence of Pt Catalysts for Propane Dehydrogenation: from Atomically Dispersed to Nanoparticles, *ACS Catal.*, 2020, **10**, 12932–12942.

32 R. Peng, S. Li, X. Sun, Q. Ren, L. Chen, M. Fu, J. Wu and D. Ye, Size effect of Pt nanoparticles on the catalytic oxidation of toluene over Pt/CeO_2 catalysts, *Appl. Catal., B*, 2018, **220**, 462–470.

33 W. J. Dong, Y. Xiao, K. R. Yang, Z. Ye, P. Zhou, I. A. Navid, V. S. Batista and Z. Mi, Pt nanoclusters on GaN nanowires for solar-asssisted seawater hydrogen evolution, *Nat. Commun.*, 2023, **14**, 179.

34 J. Wu, L.-Y. Qiao, Z.-F. Zhou, G.-J. Cui, S.-S. Zong, D.-J. Xu, R.-P. Ye, R.-P. Chen, R. Si and Y.-G. Yao, Revealing the synergistic effects of Rh and substituted $La_2B_2O_7$ (B= Zr or Ti) for preserving the reactivity of catalyst in dry reforming of methane, *ACS Catal.*, 2018, **9**, 932–945.

35 Z. Zhang, Y. Liang, H. Huang, X. Liu, Q. Li, L. Chen and D. Xu, Stable and Highly Efficient Photocatalysis with Lead-Free Double-Perovskite of $Cs_2AgBiBr_6$, *Angew. Chem., Int. Ed.*, 2019, **58**, 7263–7267.

36 Q. Y. Shen, T. Y. Xu, G. L. Zhuang, Y. Zhuang, L. M. Sun, X. G. Han, X. J. Wang and W. W. Zhan, Spatially Separated Photoinduced Charge Carriers for the Enhanced Photocatalysis Over the One-Dimensional Yolk-Shell In_2Se_3@N-C Nanoreactor, *ACS Catal.*, 2021, **11**, 12931–12939.

37 J. Low, J. Yu, M. Jaroniec, S. Wageh and A. A. Al-Ghamdi, Heterojunction photocatalysts, *Adv. Mater.*, 2017, **29**, 1601694.

38 Y. Wang, X. Rong, S. Ivanov, V. Jmerik, Z. Chen, H. Wang, T. Wang, P. Wang, P. Jin and Y. Chen, Deep ultraviolet light source from ultrathin GaN/AlN MQW structures with output power over 2 watt, *Adv. Opt. Mater.*, 2019, **7**, 1801763.

39 B. Zhou, Y. Ma, P. Ou, Z. Ye, X.-Y. Li, S. Vanka, T. Ma, H. Sun, P. Wang and P. Zhou, Light-driven synthesis of C_2H_6 from

CO_2 and H_2O on a bimetallic AuIr composite supported on InGaN nanowires, *Nat. Catal.*, 2023, **6**, 987–995.

40 S. Luo, H. Lin, Q. Wang, X. Ren, D. Hernandez-Pinilla, T. Nagao, Y. Xie, G. Yang, S. Li, H. Song, M. Oshikiri and J. Ye, Triggering Water and Methanol Activation for Solar-Driven H_2 Production: Interplay of Dual Active Sites over Plasmonic ZnCu Alloy, *J. Am. Chem. Soc.*, 2021, **143**, 12145–12153.

41 T. M. Nyathi, N. Fischer, A. P. E. York, D. J. Morgan, G. J. Hutchings, E. K. Gibson, P. P. Wells, C. R. A. Catlow and M. Claeys, Impact of Nanoparticle-Support Interactions in Co_3O_4/Al_2O_3 Catalysts for the Preferential Oxidation of Carbon Monoxide, *ACS Catal.*, 2019, **9**, 7166–7178.

42 I. Gausemel, O. H. Ellestad and C. J. Nielsen, On the use of infrared spectroscopy in the study of carbon dioxide decomposition on copper containing methanol synthesis catalysts, *Catal. Lett.*, 1997, **45**, 129–133.

43 M. Ibrahim, A. A. Shaltout, D. E. Atta, A. F. Jalbout and M. Soylak, Removal of COOH, Cd and Pb Using Water Hyacinth: FTIR and Flame Atomic Absorption Study, *J. Iran. Chem. Soc.*, 2009, **6**, 364–372.

44 J. Xu, Z. Ju, W. Zhang, Y. Pan, J. Zhu, J. Mao, X. Zheng, H. Fu, M. Yuan, H. Chen and R. Li, Efficient Infrared-Light-Driven CO_2 Reduction Over Ultrathin Metallic Ni-doped CoS_2 Nanosheets, *Angew. Chem., Int. Ed.*, 2021, **60**, 8705–8709.

45 R. Rahal, T. Pigot, D. Foix and S. Lacombe, Photocatalytic efficiency and self-cleaning properties under visible light of cotton fabrics coated with sensitized TiO_2, *Appl. Catal., B*, 2011, **104**, 361–372.

46 M. G. Kibria and Z. Mi, Artificial photosynthesis using metal/nonmetal-nitride semiconductors: current status, prospects, and challenges, *J. Mater. Chem. A*, 2016, **4**, 2801–2820.

47 W. Kohn and L. J. Sham, Self-Consistent Equations Including Exchange and Correlation Effects, *Phys. Rev.*, 1965, **140**, A1133–A1138.

48 G. Kresse and D. Joubert, From ultrasoft pseudopotentials to the projector augmented-wave method, *Phys. Rev. B: Condens. Matter Mater. Phys.*, 1999, **59**, 1758–1775.

49 G. Kresse and J. Furthmüller, Efficient iterative schemes for ab initio total-energy calculations using a plane-wave basis set, *Phys. Rev. B: Condens. Matter Mater. Phys.*, 1996, **54**, 11169–11186.

50 J. P. Perdew, J. A. Chevary, S. H. Vosko, K. A. Jackson, M. R. Pederson, D. J. Singh and C. Fiolhais, Atoms, molecules, solids, and surfaces: Applications of the generalized gradient approximation for exchange and correlation, *Phys. Rev. B: Condens. Matter Mater. Phys.*, 1992, **46**, 6671–6687.

51 J. P. Perdew, K. Burke and M. Ernzerhof, Generalized Gradient Approximation Made Simple, *Phys. Rev. Lett.*, 1996, **77**, 3865–3868.

52 P. E. Blöchl, Projector augmented-wave method, *Phys. Rev. B: Condens. Matter Mater. Phys.*, 1994, **50**, 17953–17979.

53 H. J. Monkhorst and J. D. Pack, Special points for Brillouin-zone integrations, *Phys. Rev. B: Condens. Matter Mater. Phys.*, 1976, **13**, 5188.

54 J. K. Nørskov, J. Rossmeisl, A. Logadottir, L. Lindqvist, J. R. Kitchin, T. Bligaard and H. Jónsson, Origin of the Overpotential for Oxygen Reduction at a Fuel-Cell Cathode, *J. Phys. Chem. B*, 2004, **108**, 17886–17892.

55 V. Wang, N. Xu, J.-C. Liu, G. Tang and W.-T. Geng, VASPKIT: A user-friendly interface facilitating high-throughput computing and analysis using VASP code, *Comput. Phys. Commun.*, 2021, **267**, 108033.